Electronic Supplementary Material (ESI) for ChemComm.
This journal is © The Royal Society of Chemistry 2014

Assembly of Fe-substituted Dawson-type nanoscale selenotungstates clusters with photocatalytic H_2 evolution activity

Wei-Chao Chen, Chao Qin, Xin-Long Wang, Yang-Guang Li, Hong-Ying Zang, Yan-Qing Jiao, Peng Huang, Kui-Zhan Shao, Zhong-Min Su,* and En-Bo Wang*[a]

[a]*Institute of Functional Material Chemistry, Key Lab of Polyoxometalate Science of Ministry of Education, Faculty of Chemistry, Northeast Normal University, Changchun, 130024 Jilin, People's Republic of China.*

CONTENTS

Section 1 Synthesis, Crystal Data, and Structures of 1-2

1.1 Synthesis

Materials: All chemicals and solvents were commercially purchased and used without further purification. The polyoxotungstate cluster $(NH_4)_6Na_{18}[Se_6W_{39}O_{141}(H_2O)_3]\cdot 70H_2O$ was prepared according to the literature method (*Chem. Commun.*, 2014, **50**, 2155–2157).

Synthesis of 1: $Na_2WO_4\cdot 2H_2O$ (1.70 g, 5.12 mmol) and Na_2SeO_3 (0.13 g, 0.73 mmol) were dissolved in 30 mL water. The pH value of the solution was adjusted to 4.5 by the 50% (1:1) acetic acid solution. After the solution was stirred for around 30 min, solid $Fe(NO_3)_3\cdot 9H_2O$ (0.20 g, 0.50 mmol) and dimethylamine hydrochloride (0.70 g, 6.13 mmol) were successively added. The final pH was kept at 5.5 by 4 M NaOH. This solution was stirred for another 10 min and then heated to 80 ^oC stirred for 0.5 h, cooled down to room temperature, filtered and left to evaporate slowly. Yellow block-shaped crystals were obtained after two weeks, which were then collected by filtration and air-dried. Yield: 0.34 g, (21.3 %, based on W). IR (in cm^{-1}): 3443 (w), 3136 (w), 2790 (w), 1605 (s), 1526 (m), 1464 (s), 1406 (m), 1021 (m), 954 (s), 809 (w), 746 (w). Elemental analysis, calc. for $C_8H_{136}Fe_6N_4Na_{14}O_{184}Se_6W_{34}$: C 0.91, N 0.53, Na 3.03, Fe 3.16, Se 4.46, W 58.9 %; Found C 0.79, N 0.44, Na 2.88, Fe 2.83, Se 4.68, W 59.7 %.

Synthesis of 2: $(NH_4)_6Na_{18}[Se_6W_{39}O_{141}(H_2O)_3]\cdot 70H_2O$ (0.50 g, 0.043 mmol) and NH_4Cl (0.27 g, 5.00 mmol) were dissolved with stirring in 40 ml H_2O, the reaction mixture was stirred for 30 min. Solid $Fe(NO_3)_3\cdot 9H_2O$ (0.20 g, 0.50mmol) were added, the white cloudy solution turn to orange cloudy mixture after another five minutes. This solution was heated to 100 °C stirred for 0.5 h, and then cooled to room temperature and filtered. The final pH was about 2.50. Slow evaporation of the solution results in the yellow crystals **2** forming in one month. Yield: 0.12 g, (24.8 %, based on W). IR (in cm^{-1}): 3437 (s), 1620 (s), 960 (m), 864 (s), 741 (w), 640 (m).

Elemental analysis, calc. for $H_{146}Fe_{10}N_9Na_{19}O_{286}Se_8W_{62}$: N 0.71, Na 2.44, Fe 3.12, Se 3.53, W 63.8 %; Found N 0.62, Na 2.69, Fe 3.37, Se 3.46, W 62.1 %.

1.2 Synthesis Discussion

Precise control of the one-pot reaction conditions was employed for the assembly of **1**. Many previous reports pointed that the SeO_3^{2-} anion template has a lone pair of electrons and only form three bonds through oxygen atoms in trigonal configurations, they effectively give rise to "open" lacunary units instead of "closed" Keggin-type or Dawson-type building blocks. Such templates can be viewed as "inorganic ligands".[1] The acidification of WO_4^{2-} and SeO_3^{2-} by acetic acid was necessary, because acetic acid has already been proved to be a suitable reagent for acidifying Se-based POTs clusters[1b]. Furthermore, molar ratio (W:Se molar ratio 7:1) also plays an important role that is in accordance with the basic lacunary Dawson-type fragment $\{\alpha\text{-}Se_2W_{14}\}$. Subsequently, simple metal salt, Fe^{3+}, was introduced to the acid solution. The possibly formative lacunary Dawson-type fragment $\{\alpha\text{-}Se_2W_{14}\}$ filled with the Fe centers that forms the saturated $\{M_{18}\}$ configuration which lays the foundation of the sandwich cluster $\{Fe_6Se_6W_{34}\}$. Besides, the organo-ammonium cations (dimethylamine hydrochloride)[1a, 2] were employed to restrict the aggregation of more highly symmetrical clusters during the assembly process, resulting in the successful synthesis of **1**.

Compound **2** was synthesized in moderately acidic reactions with $\{Se_6W_{39}\}$ precursor. The reported trimeric macrocyclic species $[Se_6W_{39}O_{141}(H_2O)_3]^{24-}$ possesses powerful ability to reassemble in high ionic strength media[3]. By reassembly and then refluxing a high counter cations media solution of $\{Se_6W_{39}\}$ precursor in the presence of Fe centers, we theorize that the formation of the controlled degradation of the precursor, known to be a slow process and in kinetic equilibrium[4], may lead to novel lacunary Dawson-type intermediate species as inorganic ligands suitable for substitution on the Fe centers. Here, the reaction was taken in a NH_4^+-rich media. The lacunary Dawson-type intermediate species derived from $\{Se_6W_{39}\}$ unit trend to be induced by Fe centers to access saturated $\{M_{18}\}$ configurations to get the construction

of **2**. Moreover, when Fe centers was not introduced during the synthesis, thus we only found the $\{Se_6W_{39}\}$ precursor precipitated after about two months, which deeply proved that the role of Fe centers remains indispensable, in other words, the "metal-inducing" strategy remains powerful.

References:

[1] (a) M. Hutin, D.-L. Long, L. Cronin, *Isr. J. Chem.* 2011, **51**, 205 –214; (b) J. Yan, D.-L. Long and L. Cronin, *Angew. Chem., Int. Ed.*, 2010, **49**, 4117–4120; (c) J. Gao, J. Yan, S. Beeg, D.-L. Long and L. Cronin, *J. Am. Chem. Soc.*, 2012, **135**, 1796–1805; (d) W.-C. Chen, H.-L. Li, X.-L. Wang, K.-Z. Shao, Z.-M. Su and E.-B. Wang, *Chem.–Eur. J.*, 2013, **19**, 11007–11015. (e) J. M. Cameron, J. Gao, D.-L. Long and L. Cronin, *Inorg. Chem. Front.*, 2014, **1**, 178–185; (f) L.-J. Wang, W.-J. Li, L.-Z. Wu, X.-B. Dong, H.-M. Hu and G.-L. Xue, *Inorg. Chem. Commun.*, 2013, **35**, 122-125. (g) J. Yan, J. Gao, D.-L. Long, H. N. Mirasand and L.Cronin, *J. Am. Chem. Soc.*, 2010, **132**, 11410–11411.

[2] Long, D. L.; Burkholder, E.; Cronin, L. *Chem. Soc. Rev.* **2007**, *36*, 105–121.

[3] (a) J. M. Cameron, J. Gao, L. Vilà-Nadal, D.-L. Long and L. Cronin, *Chem. Commun.*, 2014, 2155–2157; (b) I. V. Kalinina, E. V. Peresypkina, N. V. Izarova, F. M. Nkala, U. Kortz, N. B. Kompankov, N. K. Moroz, and M. N. Sokolov, *Inorg. Chem.*, 2014, **53**, 2076–2082.

[4] X.-K. Fang and M. Luban, *Chem. Commun.*, 2011, 3066–3068.

1.3 Crystal Data

Table S1. Crystal Data and Structure Refinements for **1**~**2**.

	1	**2**
Empirical formula	$C_8H_{136}Fe_6N_4Na_{14}O_{184}Se_6W_{34}$	$H_{146}Fe_{10}N_9Na_{19}O_{286}Se_8W_{62}$
M	10614.83	17874.95
λ/Å	0.71073	0.71073
T/K	296(2)	296(2)
Crystal system	Monoclinic	Monoclinic

Space group	*C2/m*	$P2_1/n$
a/Å	34.907(4)	17.6237(10)
b/Å	19.0714(16)	25.6225(15)
c/Å	17.8116(15)	37.073(2)
α/°	90	90
β/°	118.867(2)	91.5020(10)
γ/°	90	90
V/Å^3	10384.1(16)	16735.0(17)
Z	2	2
D_c/Mg m^{-3}	3.395	3.547
μ/mm^{-1}	20.336	22.620
F(000)	9428	15652
θ Range/°	2.08–25.00	1.83–25.00
Measured reflections	26971	85907
Independent reflections	9423	29399
Data/restraints/ Parameters	9423 / 53 / 326	29399 / 203 / 1632
R_{int} after SQUEEZE	0.0548	0.0701
Goodness-of-fit on F^2	0.996	0.948
$R_1(I > 2\sigma(I))$	0.0600	0.0455
wR_2 $(I > 2\sigma(I))$	0.1670	0.1123

Single-crystal X-ray diffraction: Single-crystal X-ray diffraction data for **1**~**2** were recorded on a Bruker Apex CCD II area-detector diffractometer with graphite-monochromated $Mo_{K\alpha}$ radiation (λ = 0.71073 Å) at 296(2) K. Absorption corrections were applied using multiscan technique and performed by using the SADABS program[1]. The structures of **1**~**2** were solved by direct methods and refined on F^2 by full-matrix leastsquares methods by using the SHELXTL package[2]. Anisotropic thermal parameters were used to refine all non-hydrogen atoms.

Hydrogen atoms attached to lattice water molecules were not located. The numbers of lattice water molecules and counter cations for **1**–**2** were estimated by the results of elemental analyses, TG curves, and calculations of electron count in the voids with SQUEEZE[3]. CCDC 1011424 (**1**) and 1011425 (**2**) contain the supplementary crystallographic data for this paper.

References：

[1] Sheldrick, G. *SADABS*; ver. 2.10; University of Gottingen: Göttingen, Germany, **2003**.

[2] Sheldrick, G. M. *SHELXL-97, Program for the Refinement of Crystal Structure*; University of Gottingen: Göttingen, Germany, **1993**.

[3] Spek, A. L. *PLATON, A Multipurpose Crystallographic Tool*; Utrecht University, Utrecht, The Netherlands, **2003**.

1.4 Structures of 1-2

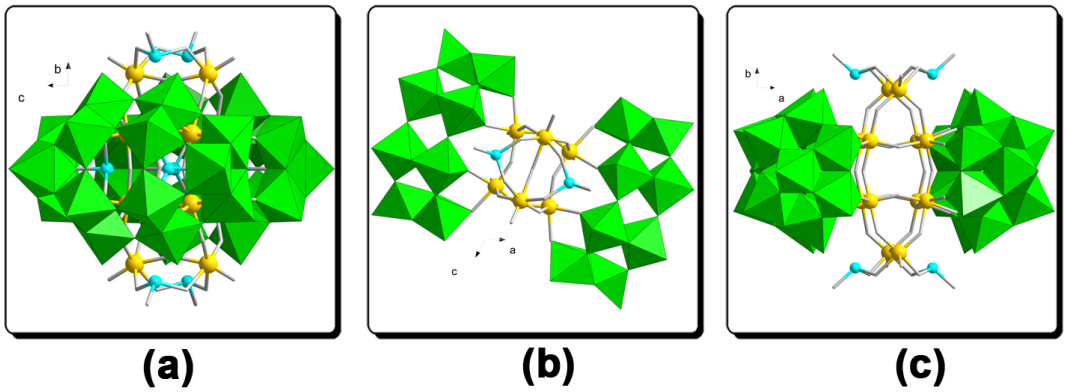

Fig. S1. Structure of **1a** in different orientations: (a) bc-view, (b) ac- view, (c) ab-view

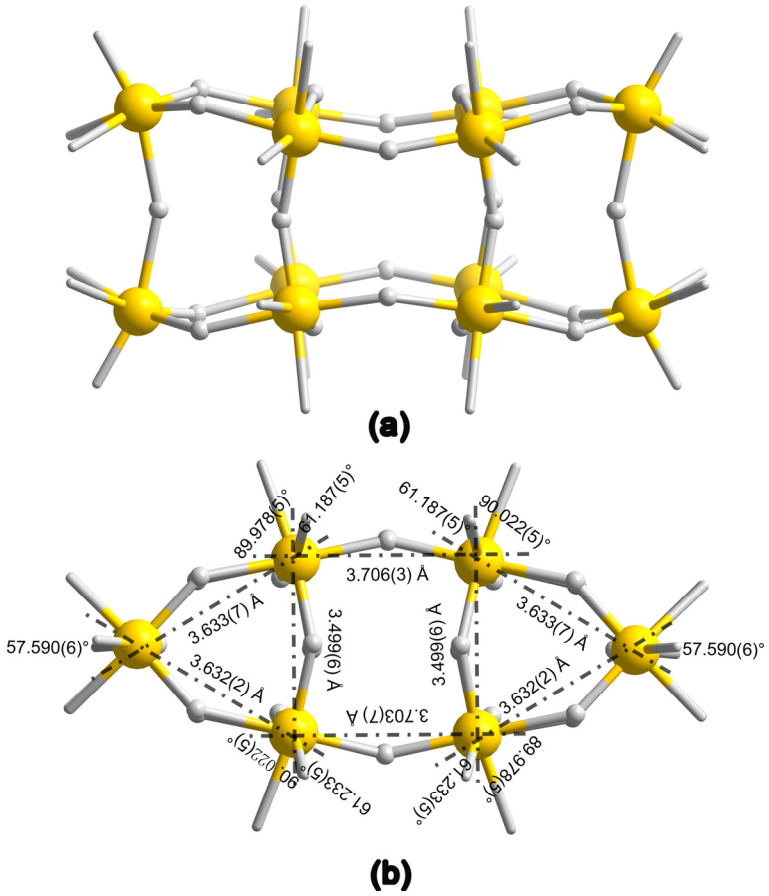

Fig. S2. Structure of the $\{Fe_6W_6\}$ unit in **1a**: (a) side-view, (b) top-view. Connection patterns of one regular cube and two triangular prism topologies (b).

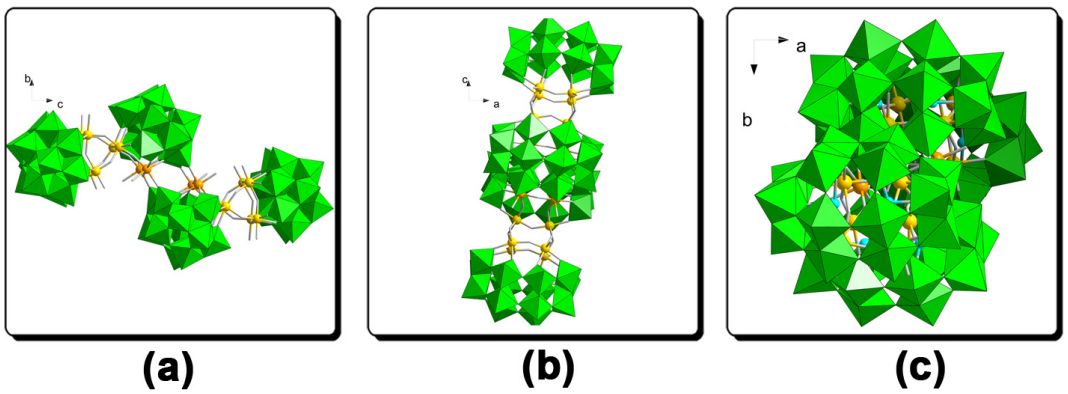

Fig. S3. Structure of **2a** in different orientations: (a) bc-view, (b) ac- view, (c) ab-view

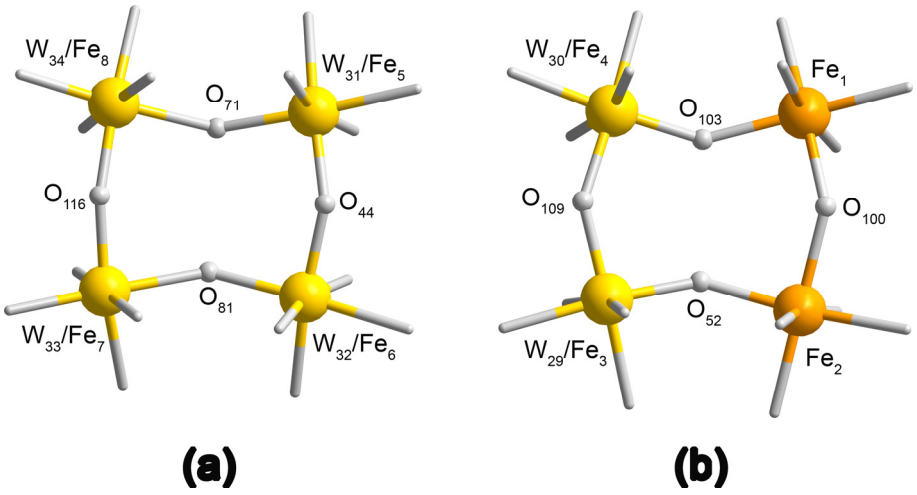

Fig. S4. Connection patterns of the $\{Fe_2W_2O_{12}\}$ unit (a) and $\{Fe_3WO_{12}\}$ unit (b) in **2a**.

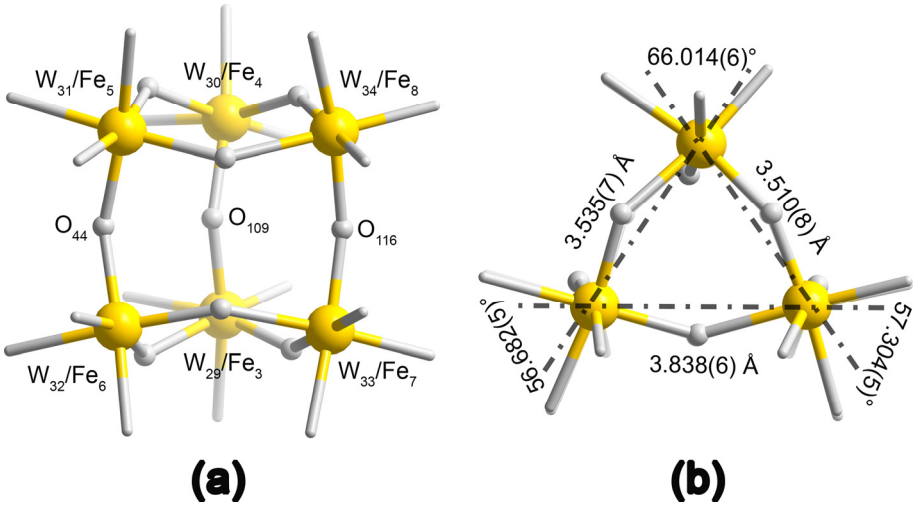

Fig. S5. Connection patterns of the regular triangular prism $\{Fe_3W_3O_9\}$ unit in **2a**. (a) front-view, (b) top-view.

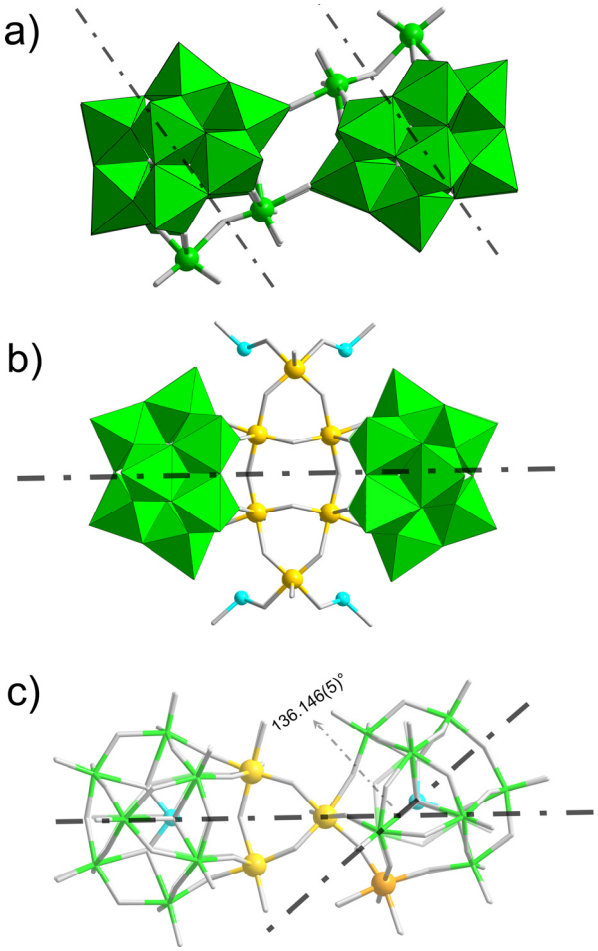

Fig. S6. The arrangements of dimeric structure $\{Se_4W_{36}\}$ (a), **1a** (b), and $\{Fe_5Se_4W_{31}\}$ in **2a** (c). Different orientation upon the saturated $\{M_{18}\}$ structures: planar alignment for $\{Se_4W_{36}\}$ (a); face to face arrangement for **1a** (b); arrangement with a angle of 134.146(5)° for **2a** (c).

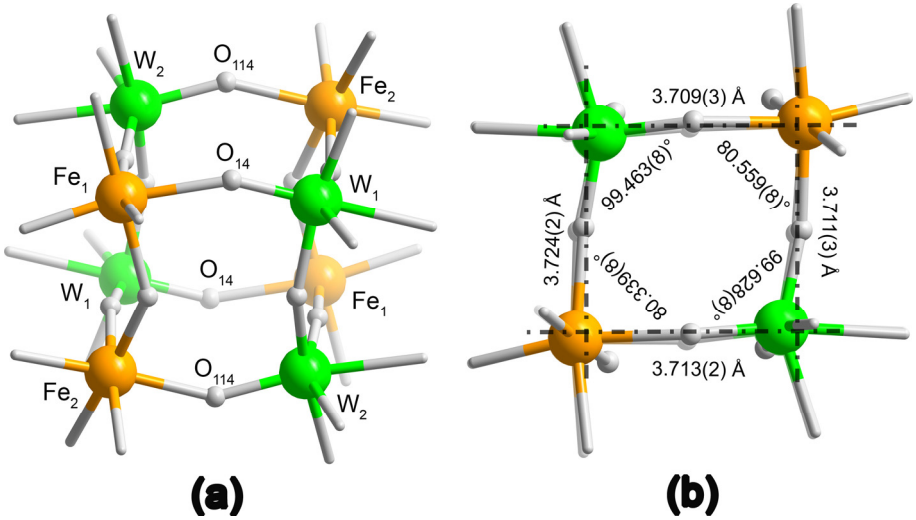

Fig. S7. Connection patterns of the regular cube $\{Fe_4W_4O_{12}\}$ unit in **2a**. (a) front-view, (b) top-view.

1.5 The BVS Calculation Result of All the Oxygen Atoms

Table S2. The BVS calculation results of all the oxygen atoms in **1**.

Oxygen Code	Bond Valence	Protonation Degree	Oxygen Code	Bond Valence	Protonation Degree
O_1	1.255	1	O_{24}	1.041	1
O_2	0.992	1	O_{27}	1.000	1
O_8	0.960	1	O_{35}	0.555	1
O_{11}	0.987	1	O_{39}	1.365	1
Total 16 protons per cluster					

Table S3. The BVS calculation results of all the oxygen atoms in **2**.

Oxygen Code	Bond Valence	Protonation Degree	Oxygen Code	Bond Valence	Protonation Degree
O_7	1.231	1	O_{82}	1.053	1
O_{31}	1.245	1	O_{92}	1.410	1
O_{48}	0.575	1	O_{94}	1.492	1
O_{60}	0.556	1	O_{100}	0.861	1
O_{62}	0.979	1			
Total 18 protons per cluster					

Table S4. The BVS calculation result of all Se^{IV} atoms in compounds **1** and **2**.

Compound **1**			
Code	Bond Valence	Code	Bond Valence
Se_1	3.814	Se_2	3.928
Se_3	3.918		
Compound **2**			
Code	Bond Valence	Code	Bond Valence
Se_1	3.913	Se_2	3.956
Se_3	4.209	Se_4	4.136

Section 2 Experimental Section

2.1 Materials and Physical Measurements

Characterization: Elemental analysis of Na, Se, W, and Fe were performed with a Leaman inductively coupled plasma (ICP) spectrometer; C and N were performed on a Perkin-Elmer 2400 CHN elemental analyzer. IR spectra were recorded on an Alpha Centauri FTIR spectrophotometer on pressed KBr pellets in the range 400~4000 cm^{-1}. Water contents were determined by TG analyses on a PerkinElmer TGA7 instrument in flowing N_2 with a heating rate of 10 °C min^{-1}. Electrospray ionization mass spectrometry was carried out on a Bruker Micro TOF-QII instrument (1 mg/mL).

Magnetic measurements: Magnetic susceptibility measurements on **1**–**2** were performed with a Quantum Design SQUID magnetometer (MPMS-XL). The dc measurements were conducted from 2.0 to 300 K at 0.1 T on polycrystalline samples. Experimental data were corrected for the sample holder and for the diamagnetic contribution of the sample, calculated from Pascal constants.

Electrochemical experiments: Electrochemical measurements were carried out on a CHI 660 electrochemical workstation at room temperature. Thrice-distilled water was used throughout the experiments. All solutions were deaerated by bubbling pure argon prior to the experiments and the electrochemical cell was kept under an argon atmosphere throughout the experiment. A conventional three-electrode system was used with a 1.5 mm glassy carbon working electrode, an Ag/AgCl used as electrode, and a platinum wire counterelectrode. The glassy carbon working electrodes were polished with alumina on polishing pads, rinsed with distilled water, and sonicated in H_2O before each experiment. The scan rate was 50~450 mV s^{-1}. All potentials were measured and reported versus Ag/AgCl. Solutions **1** and **2** in 0.5 M H_2SO_4/Na_2SO_4 (pH = 2.5) were used. A pHS-25B pH meter was used for pH measurements.

Photocatalytic Measurements: Photocatalytic reactions were carried out in a Pyrex

inner-irradiation-type reaction vessel with a magnetic stirrer at room temperature. The reactant solution was evacuated using N_2 several times to ensure complete air removal and then irradiated by using a 500 W mercury lamp. The produced H_2 was analyzed by a GC9800 instrument with a thermal conductivity detector and a 5 Å molecular sieve column (2 mm × 2 mm) using N_2 as carrier gas.

2.2 UV-Vis spectra

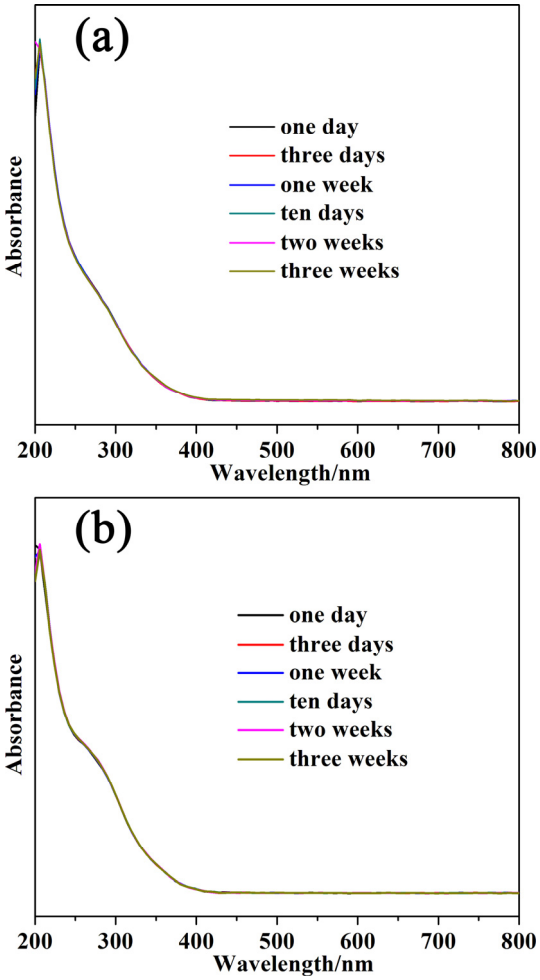

Fig. S8. UV-Vis spectra of **1** (a) and **2** (b) kept at room temperature for three weeks.

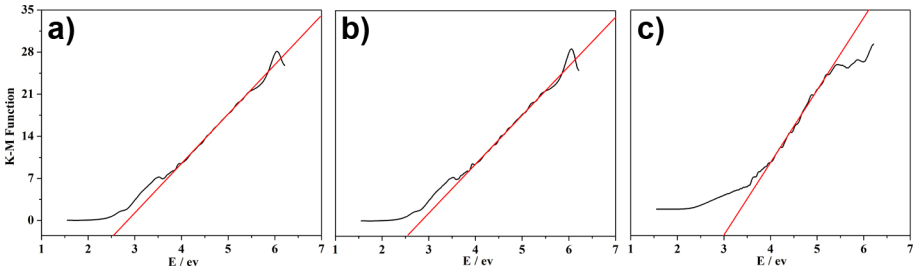

Fig. S9. The diffuse reflectance UV-vis-NIR spectra of K-M function *vs.* energy (eV) of **1** (a), **2** (b), and **{Se_4W_{36}}** (c).

2.3 ESI-MS

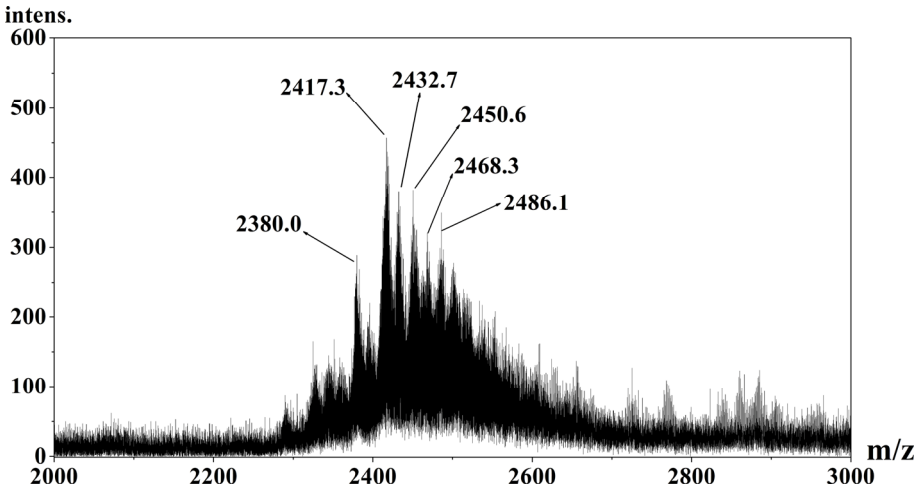

Fig. S10. ESI-MS of **1** in H_2O.

Table S5. Assignment of peaks in negative mode Mass spectrum of **1a**.

Observed m/z	Calculated m/z	Charge	Polyanion
2380.0	2380.1	-4	$\{Na_5(C_2H_8N)H_8[Fe_6Se_6W_{34}O_{124}(OH)_{16}](H_2O)_2\}^{4-}$
2417.3	2417.6	-4	$\{Na_{11}(C_2H_8N)H_2[Fe_6Se_6W_{34}O_{124}(OH)_{16}](H_2O)_3\}^{4-}$
2432.7	2433.4	-4	$\{Na_{11}(C_2H_8N)_2H[Fe_6Se_6W_{34}O_{124}(OH)_{16}](H_2O)_4\}^{4-}$
2450.6	2450.4	-4	$\{Na_{10}(C_2H_8N)_4[Fe_6Se_6W_{34}O_{124}(OH)_{16}](H_2O)_4\}^{4-}$
2468.3	2468.4	-4	$\{Na_{10}(C_2H_8N)_4[Fe_6Se_6W_{34}O_{124}(OH)_{16}](H_2O)_8\}^{4-}$
2486.1	2485.4	-4	$\{Na_9(C_2H_8N)_4H[Fe_6Se_6W_{34}O_{124}(OH)_{16}](H_2O)_{13}\}^{4-}$

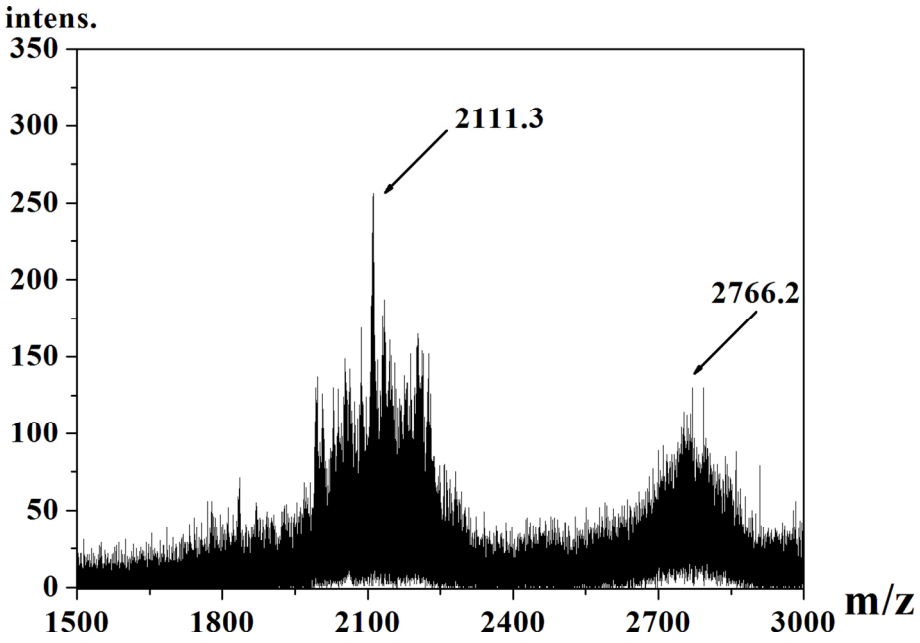

Fig. S11. ESI-MS of **2** in H_2O.

Table S6. Assignment of peaks in negative mode Mass spectrum of **2a**.

Observed m/z	Calculated m/z	Charge	Polyanion
2111.3	2111.2	-8	$\{(NH_4)_5Na_8H_7[Fe_{10}(H_2O)_4Se_8W_{62}O_{222}(OH)_{18}](H_2O)_5\}^{8-}$
2766.2	2766.3	-6	$\{(NH_4)NaH_{20}[Fe_{10}(H_2O)_4Se_8W_{62}O_{222}(OH)_{18}](H_2O)\}^{6-}$

2.4 Cyclic Voltammetry

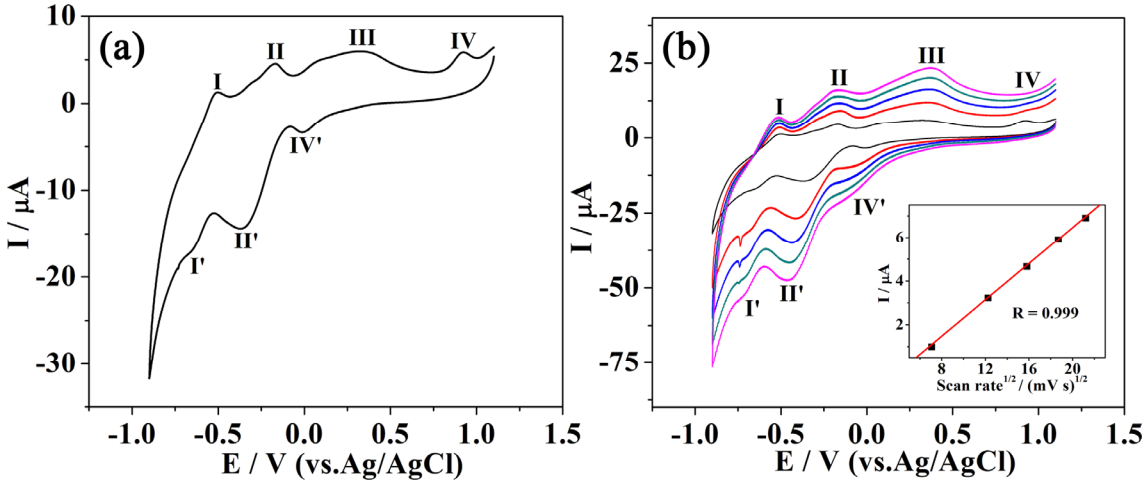

Fig. S12. Cyclic voltammograms of **1** in aqueous 0.5 M H_2SO_4/Na_2SO_4 solutions (pH = 2.50). The scan rate was 50 mV s^{-1} (a). Cyclic voltammograms of **1** at different scan

rates (b): from inside to out: 50, 150, 250, 350 and 450 mV s^{-1}. Inset: representation of the current as a function of the square root of the scan rate. The linear relationship indicates that the processes are diffusion controlled. The working electrode was glassy carbon, and the reference electrode was Ag/AgCl.

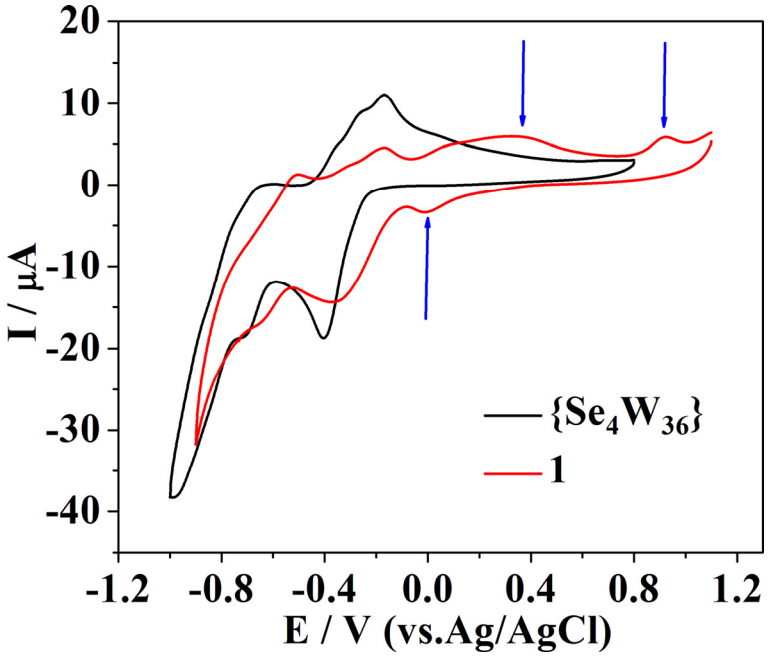

Fig. S13. Cyclic voltammograms of **1** (red) and $\{Se_4W_{36}\}$ (black) in 0.5 M H_2SO_4/Na_2SO_4 solution (pH = 2.50). The scan rate was 50 mV s^{-1}. The working electrode was glassy carbon, and the reference electrode was Ag/AgCl.

Table S7. Redox Peak Potentials for all the Tungsten Waves Determined by Cyclic Voltammetry in 0.5 M H_2SO_4/Na_2SO_4 solution (pH = 2.50) for **1** and **$\{Se_4W_{36}\}$**.

	E_{pa} (V)	E_{pc} (V)	$E_{1/2}$ (V)
1	−0.175	−0.352	−0.264
	−0.510	−0.649	−0.580
$\{Se_4W_{36}\}$	−0.156	−0.419	−0.288
	−0.656	−0.718	−0.687

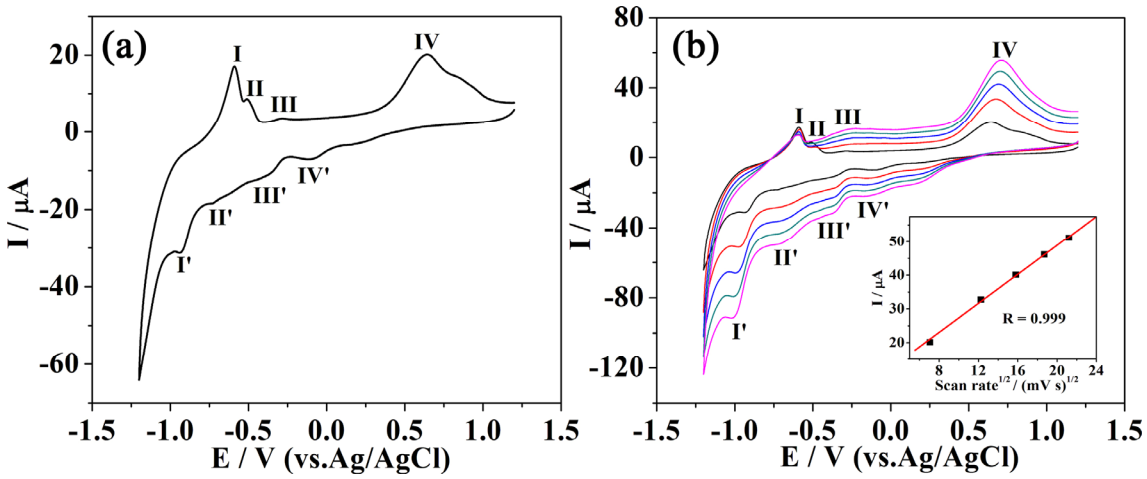

Fig. S14. Cyclic voltammograms of **2** in aqueous 0.5 M H_2SO_4/Na_2SO_4 solutions (pH = 2.50). The scan rate was 50 mV s^{-1} (a). Cyclic voltammograms of **2** at different scan rates (b): from inside to out: 50, 150, 250, 350 and 450 mV s^{-1}. Inset: representation of the current as a function of the square root of the scan rate. The linear relationship indicates that the processes are diffusion controlled. The working electrode was glassy carbon, and the reference electrode was Ag/AgCl.

Table S8. Redox Peak Potentials for all the Tungsten Waves Determined by Cyclic Voltammetry in 0.5 M H_2SO_4/Na_2SO_4 solution (pH = 2.50) for **2**.

	E_{pa} (V)	E_{pc} (V)	$E_{1/2}$ (V)
	−0.296	−0.362	−0.329
2	−0.518	−0.733	−0.626
	−0.599	−0.943	−0.771

Electrochemistry: Cyclic voltammetry (CV) experiments were performed to examine the redox properties of **1** and **2** in 0.5 M H_2SO_4/Na_2SO_4 solutions pH = 2.50. All of the two compounds show the waves associated with the reduction of W^{VI} centers between –0.943 and –0.352 V as well as the redox process of Fe^{III} centers from –0.116 to +0.919 V (*vs* Ag/AgCl), which are in good agreement with reported Fe^{III}-containing POT compounds.[1] In a sulfate pH 2.50 medium, the CV of **1** (Fig. S12) at a scan rate of 50 mV s^{-1} shows the main characteristic peaks associated with W

centered redox couples in the region −0.175 V to −0.649 V of potential values *vs* Ag/AgCl. Two separated redox couples of waves at $E_{1/2}$ = –0.580 V (I/I') and $E_{1/2}$ = –0.264 V (II/II') [$E_{1/2} = (E_{pa} + E_{pc})/2$], corresponding to the redox processes of W^{VI} centers, respectively (Tab. S6). Also, Fig. S13 compares the CVs of **1** and the $[(Se_2W_{18}O_{60})_2(\mu_2\text{-}O)_4]^{16-2}$ recorded in 0.5 M H_2SO_4/Na_2SO_4 solution (pH 2.5, scan rate was 50 mV s^{-1}). This study might allow us to extract some distinct features of **1**, which is due to the introduction of Fe^{III} centers and the extra coordinate Se^{IV} centers. In the cathodic branch of the CV of **1**, it can be observed a reduction peak located at –0.028 V (IV') *vs* Ag/AgCl, which does not exist in the pattern of the $[(Se_2W_{18}O_{60})_2(\mu_2\text{-}O)_4]^{16-}$ (Fig. S13). This wave is assigned to the reduction of the Fe^{III} centres. As a matter of fact, the Fe^{III} centres are known to be more easily reduced than the W^{VI} centers as seen in several Fe^{III}-containing POTs.[1e,3] In the positive region of potentials, there are also two oxidation peaks that does not exist in the pattern of the $[(Se_2W_{18}O_{60})_2(\mu_2\text{-}O)_4]^{16-}$, it should be identified: one wave appears at about +0.919 V (IV)[1d,1e], which is attributed to the oxidation of free Fe^{II}; the other peak located at +0.378 V (III) can be assigned to the oxidation of Se^{IV}.[2,4] The extra disorder coordinated Se^{IV} centers contributes the conspicuous oxidation waves, which can be recognized in **1** while hardly to be found in $[(Se_2W_{18}O_{60})_2(\mu_2\text{-}O)_4]^{16-}$. After increasing the scan rates from 50 to 450 mV s^{-1} (Fig. S12b), the Se^{IV}-based oxidation waves gradually enhance while the Fe^{II}-based oxidation waves show a weaken trend, and the peak positions remain no shifts as described in the literature for other POMs.[5] Above 100 mV s^{-1} the peak currents were proportional to the square root of the scan rate, demonstrating that the redox process becomes diffusion-controlled, similar behaviors were observed in the case of **2** (Fig. S12b and S14b). Furthermore, similar Fe^{III}-waves also occur in the CV of **2**: the oxidation wave appeared at about +0.644 V (IV) and the reduction peak located at –0.116 V (IV') (*vs* Ag/AgCl). Fig. S14 shows the main characteristic peaks associated with W centered redox couples of **2** in the region –1.200 to +1.200 V of potential values *vs* Ag/AgCl at a scan rate of 50 mV s^{-1}. Scanning toward the negative region of potential values, the reduction of W centers occurs through three redox couples, with the corresponding $E_{1/2}$ peak potentials

located at −0.329 (III/III'), −0.626 (II/II'), and −0.771 V (I/I') (*vs* Ag/AgCl) (Tab. S7), respectively. It is well-known for the electrochemical behavior of the majority of the POMs that the number and the characteristics of these W waves depend on the pH and the buffering strength of the electrolyte.[5]

References：

[1] (a) T. M. Anderson, X. Zhang, K. I. Hardcastle and C. L. Hill, *Inorg. Chem.*, 2002, **41**, 2477–2488; (b) I. M. Mbomekalle, B. Keita, L. Nadjo, P. Berthet, K. I. Hardcastle, C. L. Hill and T. M. Anderson, *Inorg. Chem*., 2003, **42**, 1163–1169; (c) B. Keita, I. M. Mbomekalle, L. Nadjo, T. M. Anderson and C. L. Hill, *Inorg. Chem.*, 2004, **43**, 3257–3263; (d) B. Godin, Y.-G. Chen, J. Vaissermann, L. Ruhlmann, M. Verdaguer and P. Gouzerh, *Angew. Chem., Int. Ed.,* 2005, **44**, 3072–3075; (e) S. S. Mal, M. H. Dickman, U. Kortz, A. M. Todea, A. Merca, H. Bögge, T. Glaser, A. Müller, S. Nellutla, N. Kaur, J. van Tol, N. S. Dalal, B. Keita and Louis Nadjo, *Chem.–Eur. J.*, 2008, **14**, 1186–1195; (f) A. H. Ismail, B. S. Bassil, G. H. Yassin, B. Keita and U. Kortz, *Chem.–Eur. J.*, 2012, **18**, 6163–6166.

[2] W.-C. Chen, L.-K. Yan, C.-X. Wu, X.-L. Wang, K.-Z. Shao, Z.-M. Su and E.-B. Wang, *Cryst. Growth Des.*, 2014, DOI: 10.1021/cg500719q.

[3] (a) J. E. Toth, F. C. Anson, *J. Electroanal. Chem.* 1989, **256**, 361–370; (b) B. Keita, A. Belhouari, L. Nadjo, R. Contant, *J. Electroanal. Chem.* 1998, **442**, 49–57.

[4] (a) W.-C. Chen, H.-L. Li, X.-L. Wang, K.-Z. Shao, Z.-M. Su and E.-B. Wang, *Chem.–Eur. J.*, 2013, **19**, 11007–11015; (b) J. M. Cameron, J. Gao, L. Vilà-Nadal, D.-L. Long and L. Cronin, *Chem. Commun.*, 2014, 2155–2157; (c) J. M. Cameron, J. Gao, D.-L. Long and L. Cronin, *Inorg. Chem. Front.*, 2014, **1**, 178–185.

[5] (a) Jabbour, D.; Keita, B.; Mbomekalle, I. M.; Nadjo, L.; Kortz, U. *Eur. J. Inorg. Chem.* **2004**, 2036. (b) Bi, L.-H.; Wang, E.-B.; Peng, J.; Huang, R.-D.; Xu, L.; Hu, C.-W. *Inorg. Chem.* **2000**, *39*, 671. (c) Bassil, B. S.; Kortz, U.; Tigan, A. S.; ClementeJuan, J. M.; Keita, B.; Oliveira, P.; Nadjo, L. *Inorg. Chem.* **2005**, *44*, 9360. (d) Mbomekalle, I. M.; Keita, B.; Nierlich, M.; Kortz, U.; Berthet, P.; Nadjo, L. *Inorg. Chem.* **2003**, *42*, 5143. (e) Keita, B.; Lu, Y.-W.; Nadjo, L.; Contant, R. *Electrochem. Commun.* **2000**, *2*, 720.

2.5 Magnetism

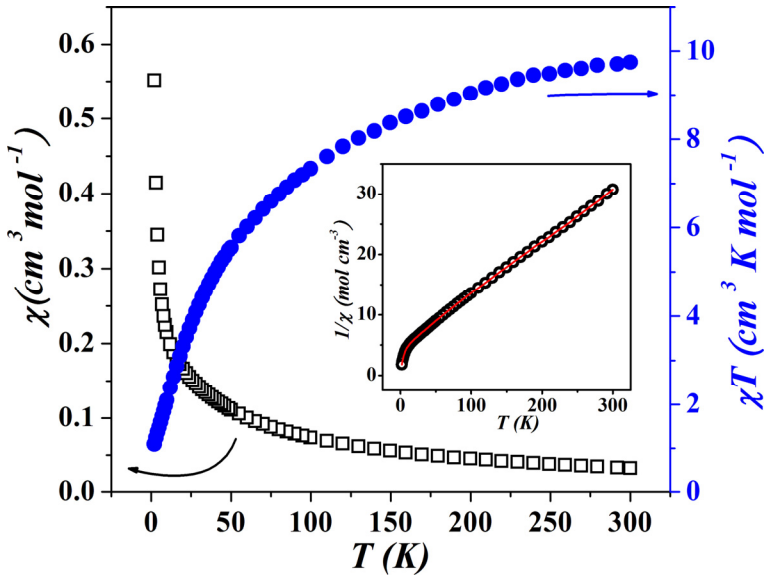

Fig. S15. χ and χT *vs* T curves of **1** (insert: $1/\chi$ *vs* T curve).

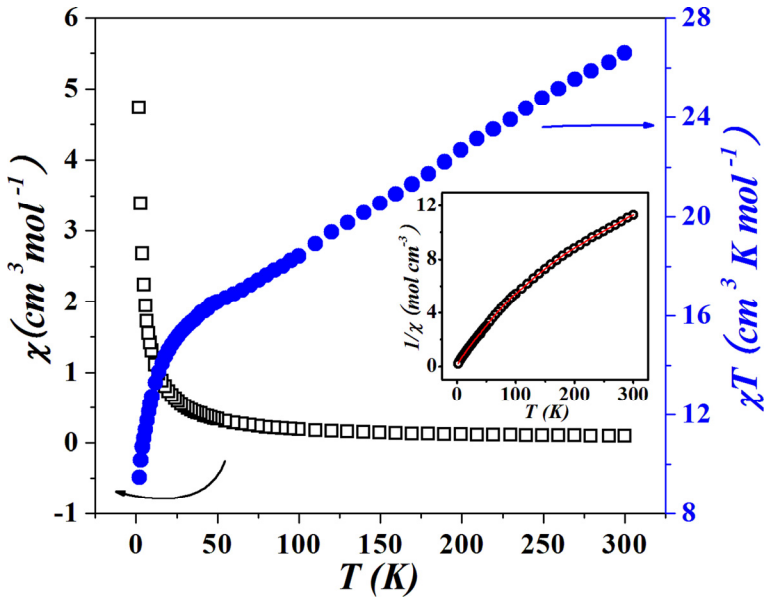

Fig. S16. χ and χT *vs* T curves of **2** (insert: $1/\chi$ *vs* T curve).

Magnetism: The DC magnetic susceptibilities χ_M of **1**–**2** were measured in the temperature range of 2.0–300 K in a 0.1 T magnetic field. Their magnetic properties are in good agreement with reported Fe^{III}-containing POT clusters.[1] The plots of χ and χT versus T (Fig. S15 and S16) reveal similar magnetic behaviours because of the

similar triangular prism Fe-topologies. As for **1**, the value of χ slowly increases from 3.25×10^{-2} cm^3 mol^{-1} at 300 K to 0.15 cm^3 mol^{-1} at 25 K and then exponentially to the maximum of 0.55 cm^3 mol^{-1} at 2 K. At 300 K the value of χT value (9.74 cm^3 K mol^{-1}) is still significantly below the expected high-temperature limit of 26.25 cm^3 K mol^{-1} for six Fe^{III} centers (S = 5/2, assuming g = 2.0), indicating antiferromagnetic interactions[1b]. In addition, the $1/\chi$ versus T curve (insets in Fig. S15) is in accordance with the Curie–Weiss law in high temperature region, yielded a Curie constant of C = 11.65 cm^3 K mol^{-1} and a Weiss constant θ of −57.24 K, which consolidates the presence of antiferromagnetic coupling within Fe^{III} centers. Similar situation also occurs in **2**: at room temperature the χT value of 26.59 cm^3 K mol^{-1} is lower than the calculated χT value of 43.75 cm^3 K mol^{-1} for ten high-spin Fe^{III} (S = 5/2, assuming g = 2.0) centers, indicating antiferromagnetic interactions. Moreover, the $1/\chi$ versus T curve (insets in Fig. S16) is in accordance with the Curie–Weiss law in high temperature region, yielded a Curie constant of C = 39.89 cm^3 K mol^{-1} and a Weiss constant θ of −151.64 K, the large and negative value of θ indicates a dominant antiferromagnetic coupling interaction between the Fe^{III} centers.

References:

[1] (a) B. Godin, Y.-G. Chen, J. Vaissermann, L. Ruhlmann, M. Verdaguer and P. Gouzerh, *Angew. Chem., Int. Ed.,* 2005, **44**, 3072–3075; (b) C. P. Pradeep, D.-L. Long, P. Kögerler and L. Cronin, *Chem. Commun.*, 2007, 4254–4256; (c) S. S. Mal, M. H. Dickman, U. Kortz, A. M. Todea, A. Merca, H. Bögge, T. Glaser, A. Müller, S. Nellutla, N. Kaur, J. van Tol, N. S. Dalal, B. Keita and Louis Nadjo, *Chem.–Eur. J.*, 2008, **14**, 1186–1195; (d) A. H. Ismail, B. S. Bassil, G. H. Yassin, B. Keita and U. Kortz, *Chem.–Eur. J.*, 2012, **18**, 6163–6166; (e) P. I. Molina, H. N. Miras, D.-L. Long and L. Cronin, Dalton Trans., 2014, **43**, 5190-5199. (f) J.-W. Zhao, Q.-X. Han, D.-Y. Shi, L.-J. Chen, P.-T. Ma, J.-P. Wang, J.-Y. Niu. J. Sol. St. Chem., 2011, **184**, 2756–2761.

Section 3 Supplementary Physical Characterizations

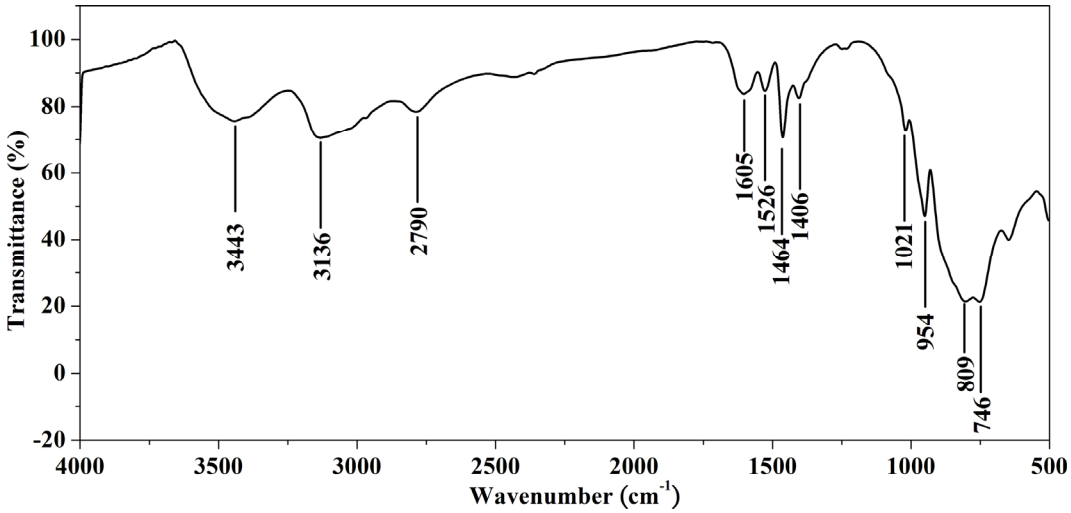

Fig. S17. IR spectrum of **1**: The characteristic peaks at 1021, 954, 809, and 746 cm^{-1} are ascribed to vibrations of ν(Se–O), ν(W=Od), ν(W–Ob), and ν(W–Oc), respectively. The broad peak at 3443 cm^{-1} and the strong peak at 1605 cm^{-1} are attributed to the lattice water molecules and aqua ligands. The peaks at 3136, 2790, 1526, 1464, and 1406 cm^{-1} are assigned to $\{C_2H_8N\}$ organic molecules.

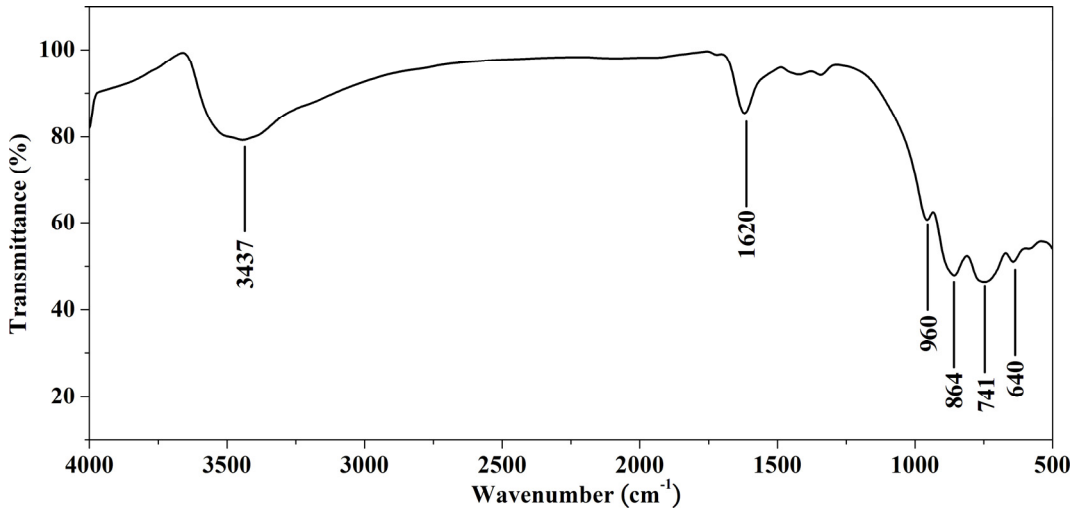

Fig. S18. IR spectrum of **2**: The characteristic peaks at 960, 864, 741, and 640 cm^{-1} are ascribed to vibrations of ν(Se–O), ν(W=Od), ν(W–Ob), and ν(W–Oc), respectively. The broad peak at 3437 cm^{-1} and the strong peak at 1620 cm^{-1} are attributed to the lattice water molecules and aqua ligands.

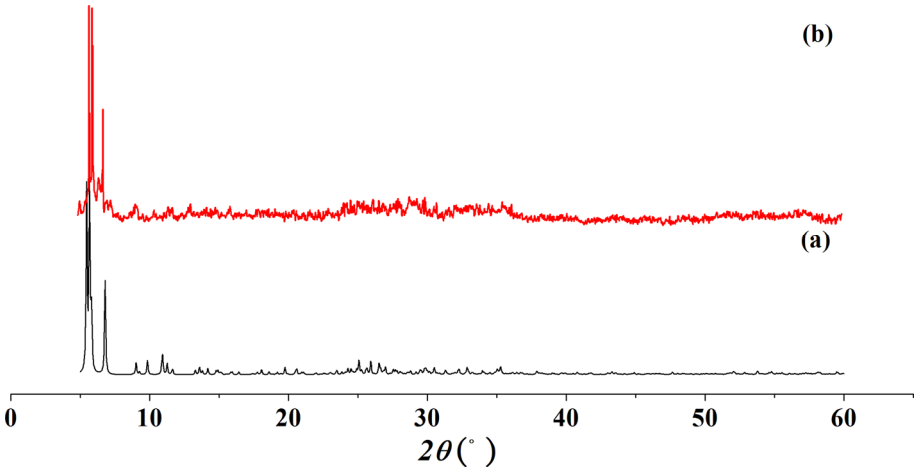

Fig. S19. The XRPD patterns for simulated (a) and as-synthesized (b) of **1**.

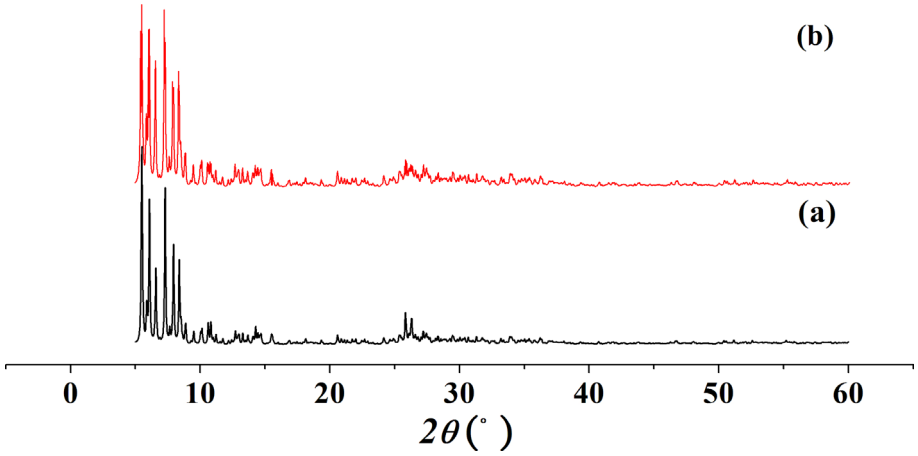

Fig. S20. The XRPD patterns for simulated (a) and as-synthesized (b) of **2**.

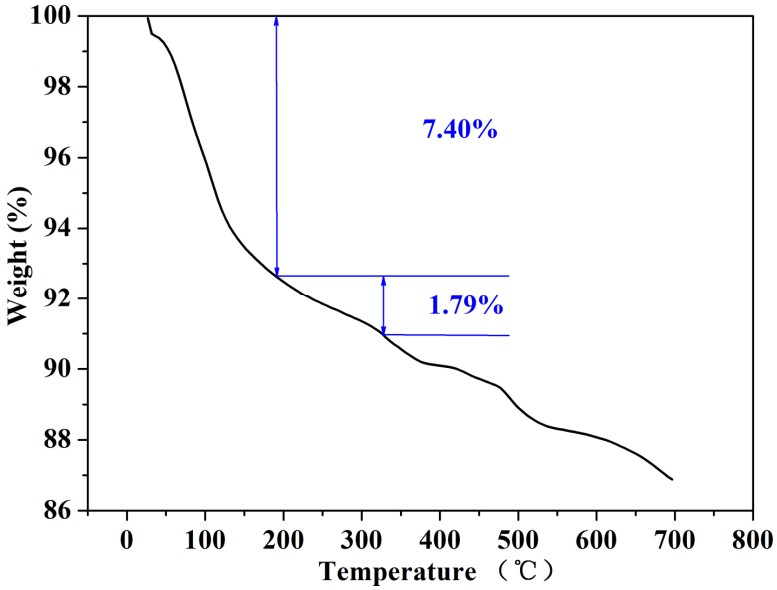

Fig. S21. TG curve of **1**. The first weight loss is in the temperature range of 50 ~ 200 °C. The value of ca. 7.40 % is in accordance with the calculated value of 7.46 % (~ $44H_2O$). The second weight loss in the temperature range of 200 ~ 300 °C is attributed to the loss of all $\{C_2H_8N\}$ organic cations. The value of 1.79 % is close to the calculated value of 1.73 % (~$4\{C_2H_8N\}$). Then the structure begins to decompose.

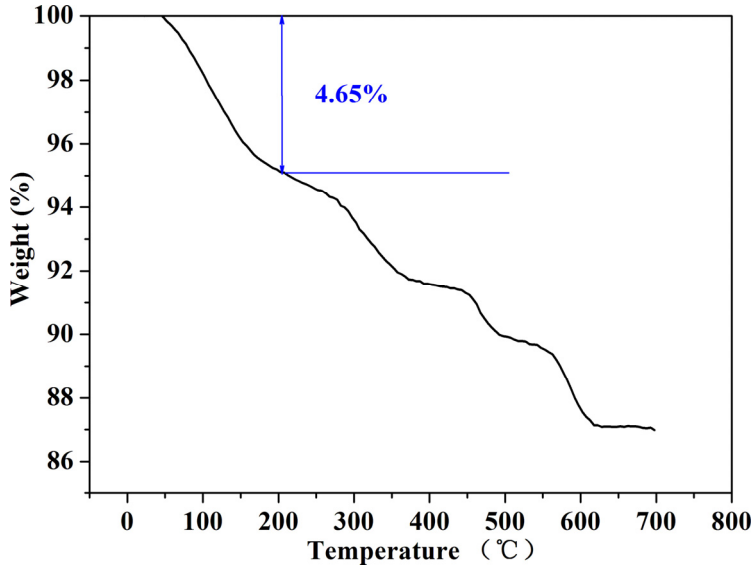

Fig. S22. TG curve of **2**. The first weight loss is in the temperature range of 50 ~ 200 °C. The value of ca. 4.65% is in accordance with the calculated value of 4.63 % (~$46H_2O$). Then the structure begins to decompose.